Spin Transition in Arrays of Gold Nanoparticles and Spin Crossover Molecules

Edwin J. Devid,[†,▼] Paulo N. Martinho,[‡,∥,▼] M. Venkata Kamalakar,[§,▼] Ivan Šalitroš,[∥,◇,▼] Úna Prendergast,[⊥,▼] Jean-François Dayen,[#] Velimir Meded,[∥] Tibebe Lemma,[⊥] Rodrigo González-Prieto,[∥,¶] Ferdinand Evers,[∥,△] Tia E. Keyes,[⊥] Mario Ruben,[∥,#] Bernard Doudin,[#] and Sense Jan van der Molen[*,†]

[†]Huygens-Kamerlingh Onnes Laboratory, Leiden Institute of Physics, Leiden University P.O. Box 9504, 2300 RA Leiden, The Netherlands, [‡]Centro de Química e Bioquímica (CQB), Faculdade de Ciências, Universidade de Lisboa, Campo Grande, 1749-016 Lisboa, Portugal, [§]Department of Microtechnology and Nanoscience, Chalmers University of Technology, SE-41296 Göteborg, Sweden, [∥]Institute of Nanotechnology, Karlsruhe Institute of Technology (KIT), Hermann-von-Helmholtz-Platz 1, 76344 Eggenstein-Leopoldshafen, Germany, [◇]Department of Inorganic Chemistry, Faculty of Chemical and Food Technology, Slovak University of Technology, Radlinskeho 9, SK-812 37, Bratislava, Slovakia, [⊥]School of Chemical Sciences, Dublin City University, Dublin 9, Ireland, [#]Institut de Physique et Chimie des Matériaux de Strasbourg (IPCMS), CNRS UMR 7504, Laboratory NIE, Université de Strasbourg, 23 Rue du Loess, 67034 Strasbourg, France, [¶]Departamento de Química Inorgánica, Facultad de Ciencias Químicas, Universidad Complutense de Madrid, Ciudad Universitaria, E-28040 Madrid, Spain, and [△]Institut für Theorie der Kondensierten Materie, Karlsruhe Institute of Technology (KIT), Wolfgang-Gaede-Straße 1, D-76128 Karlsruhe, Germany. [▼]These authors contributed equally to this work.

ABSTRACT We investigate if the functionality of spin crossover molecules is preserved when they are assembled into an interfacial device structure. Specifically, we prepare and investigate gold nanoparticle arrays, into which room-temperature spin crossover molecules are introduced, more precisely, $[Fe(AcS\text{-}BPP)_2](ClO_4)_2$, where AcS-BPP = (*S*)-(4-{[2,6-(dipyrazol-1-yl)pyrid-4-yl]ethynyl}phenyl)ethanethioate (in short, $Fe(S\text{-}BPP)_2$). We combine three complementary experiments to characterize the molecule–nanoparticle structure in detail. Temperature-dependent Raman measurements provide direct evidence for a (partial) spin transition in the $Fe(S\text{-}BPP)_2$-based arrays. This transition is qualitatively confirmed by magnetization measurements. Finally, charge transport measurements on the $Fe(S\text{-}BPP)_2$-gold nanoparticle devices reveal a minimum in device resistance *versus* temperature, $R(T)$, curves around 260–290 K. This is in contrast to similar networks containing passive molecules only that show monotonically decreasing $R(T)$ characteristics. Backed by density functional theory calculations on single molecular conductance values for both spin states, we propose to relate the resistance minimum in $R(T)$ to a spin transition under the hypothesis that (1) the molecular resistance of the high spin state is larger than that of the low spin state and (2) transport in the array is governed by a percolation model.

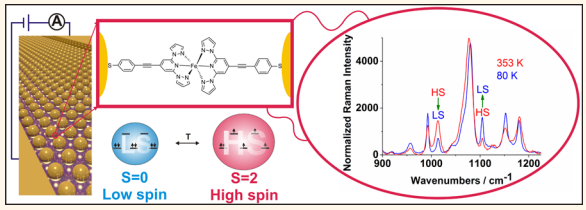

KEYWORDS: gold nanoparticles · spin crossover molecules · molecular charge transport devices · self-assembly · two-dimensional arrays

One of the most exciting prospects of molecular electronics is that future nanoscopic devices may be based on molecules with a well-defined functionality. Among the most prominent examples are molecular rectifiers[1,2] and switchable molecular devices.[3−6] Indeed, molecular switches based on a variety of mechanisms have been considered for applications. These include mechanically interlocked switches (rotaxanes, catenanes), photochromic molecules (diarylethenes, diazobenzenes), tautomerization switches, and redox-active molecules. To drive switching at the device level typically requires molecular assembly at a solid interface (*i.e.*, electrodes). *A priori*, it is difficult to judge if a switchable molecule will retain its function once it is inserted in a metal–molecule–metal device. Connecting electrodes to a molecule may affect the molecule's mechanical freedom, alter its precise density of states, and/or influence the decay of the excited state initiating the switching process. Nevertheless, a growing number of proof-of-principle switchable devices, based on bistable molecules, have been presented in the literature.[6] Here, we concentrate on molecules with a bistability related to the other basic property of the electron besides charge, such as its spin. Specifically, spin crossover (SCO) molecules are studied, with

* Address correspondence to molen@physics.leidenuniv.nl.

Received for review February 17, 2015 and accepted April 2, 2015.

Published online April 02, 2015
10.1021/acsnano.5b01103

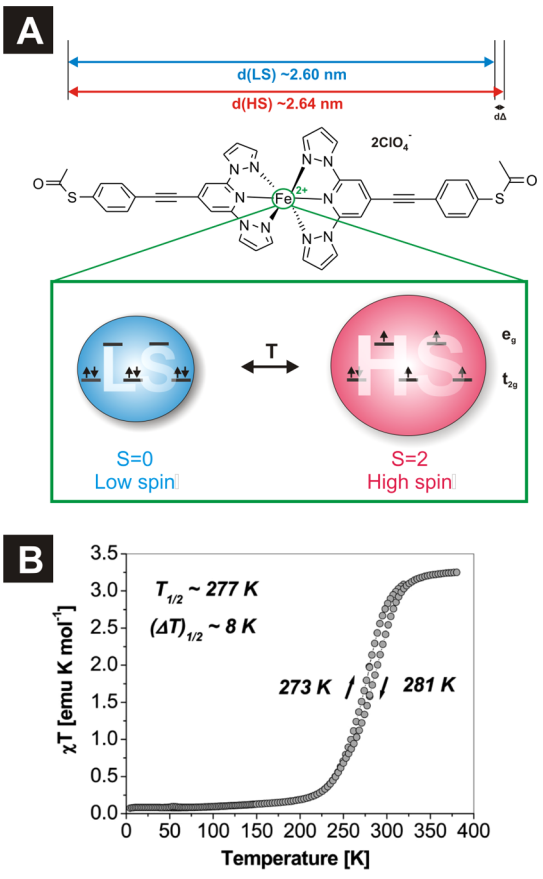

Figure 1. Spin crossover molecule 1: (A) Schematic representation of molecule 1 visualizing its spin transition (governed by the occupancy of the t_{2g} and e_g states) and the corresponding tiny length change. (B) Temperature-dependent magnetic susceptibility measurement of the same bulk crystalline SCO compound. The spin transition temperature is centered at $T_{1/2}$ = 277 K and accompanied by a thermal hysteresis loop with $\Delta T_{1/2}$ = 8 K.

the aim of finding a signature of molecular spin transition in an interfacial device geometry.

SCO molecules generally consist of a central transition metal ion, coupled to organic ligands.[4,5,7] Depending on the specific geometry and the strength of the ligand field, such molecules may switch between a diamagnetic, low-spin (LS) and a paramagnetic high-spin (HS) state as a function of temperature, illumination, pressure, and magnetic or electric field.[8−15] To illustrate this principle, Figure 1 shows the molecular species synthesized for this study, $[Fe(AcS\text{-}BPP)_2](ClO_4)_2$ (where AcS-BPP denotes (*S*)-(4-{[2,6-(dipyrazol-1-yl)pyrid-4-yl]ethynyl}phenyl)ethanethioate). Basically, a rod-like metal complex is displayed, based on an iron(II) ion and two organic ligands.[16] In bulk powder form, the formula is $[Fe(AcS\text{-}BPP)_2](ClO_4)_2$ (hereafter called molecule **1**), including thioacetate protecting groups and counterions. After exposure to gold surfaces, deprotection of the Ac−S anchor groups occurs, leading to a formal composition of $Fe(S\text{-}BPP)_2$ under near surface conditions (hereafter called molecule **1′**). The bulk sample of **1** exhibits a spin transition as illustrated by a measurement of the magnetic susceptibility χT. Plotting χT *versus* temperature *T* indicates a broad, but distinct, transition between an $S = 0$ (diamagnetic) and an $S = 2$ (paramagnetic) state (see Figure 1B). Moreover, the transition is hysteretic due to intermolecular interaction ("cooperativity") in the bulk lattice.[7]

While SCO compounds have been synthesized and studied in bulk since the 1930s,[8,9] the research activity in this field has intensified in recent years. On the one hand, prospective applications motivate scientists to increase the transition temperature up to ambient by synthesizing new molecules.[17,18] On the other hand, decreasing the size of the molecular system from macroscopic (bulk) down to nanometer scale can provide unique insight into fundamentals of spin transition properties, with applications to nanoelectronics and spintronics. The switching properties of SCO compounds may be strongly modified at the nanoscale, however. It is known that the characteristics of SCO compounds depend critically on the identity of the transition metal ion, the nature of the ligands, and the exact symmetry and strength of the ligand field.[19,20] Clearly, some of these properties may change drastically when decreasing the dimensions of ensembles of SCO molecules and their environment. Recently, scanning tunneling microscopy (STM) experiments performed on ultrathin films at low temperatures revealed that electric-field-induced switching can only occur in the second molecular layer[21] or for molecules electronically decoupled from the substrates.[22] Even though the interpretation of STM images is challenging, there are experimental indications that SCO ultrathin films exhibit transition properties deviating significantly from the bulk, in particular, by exhibiting coexistence of HS and LS states at low temperatures.[23] Molecular devices at low temperatures involving a single or a few SCO molecules were also reported by Meded *et al.*, who used a gate-controlled three-terminal molecular device to reveal possible voltage-induced switching.[15] In addition, surface spectroscopy techniques (XAS, UPS, IPES) are well-suited to characterize ultrathin films. While these ensemble-based techniques are challenged by detection sensitivity issues, they do allow for temperature-dependent studies. Bernien *et al.*[24] showed that submonolayer films with small energy coupling with the substrate preserved the bulk properties. Furthermore, Zhang *et al.*[25] reported that the substrate ferroelectric state can constrain the stable state of SCO films of several nanometers thick, and recently, photothermal switching of Fe(II) spin crossover@silica−gold nanocomposites was reported.[26] Finally, Warner *et al.*[27] performed X-ray absorption spectroscopy on submonolayers of iron complexes on flat Au(111). They found evidence for both a light- and temperature-induced spin transition but only for a fraction of the molecules. The authors argue that the precise molecular behavior depends sensitively on the interactions with the surface and with other molecules.

Upon review of the scientific literature, the question as to if and how spin transition persists in nanoscale ensembles remains open, with strong experimental indications that interactions with the substrates, or connecting electrodes, play a decisive role in the preservation or not of spin transition. Since this issue is of fundamental importance, validating the occurrence of a SCO transition is key if we want to use this type of molecule in functional devices. We propose the following two criteria for convincing experiments:

(1) the experimental insight should not rely on a single technique only. In other words, the electrical transport properties should be complemented by other methods, validating, in particular, the occurrence of a spin transition and (ideally) providing structural insight into the interaction of the SCO molecules to the substrate.

(2) temperature-dependent studies must be performed. Temperature is the best indicator of thermodynamic stability of a given phase, probing the cooperativity of the system and providing a direct comparison with known bulk properties. Previous experimental approaches to SCO molecular transport provided limited insight into temperature dependence, and most published results investigate switching of SCO molecules through a stimulus (electric field) undocumented for thin films or bulk materials.

The aim of this present work is therefore to perform temperature-dependent studies of the transition behavior of SCO molecular device structures, combining Raman spectroscopy, magnetometry, and electrical transport measurements, complemented by charge transport calculations.

We make use of two-dimensional (2D) arrays of molecular-bound Au nanoparticles, bridging the gap separating the molecular length scale and patterned metallic electrodes with typical sizes. As a basic structure, we use samples made of alkanethiol-protected gold nanoparticles. With an exchange process based on self-assembly, the molecules **1** (Figure 1) are inserted onto and between the nanoparticles. In this way, an ensemble is created based on single nanoparticle–molecule–nanoparticle junctions.[28−31] The arrays thus prepared are structurally robust at room temperature, capable of withstanding temperature sweeps, and easily addressable by external stimuli. Moreover, they allow for (control) experiments to check the device properties before and after molecular insertion. These may include several varieties of optical spectroscopy, representing an important advantage over true single-molecule techniques. At a density of junctions on the order of 10^4 per μm^2, the device architecture chosen provides direct statistical information on molecular junction properties. Still, as in most molecular device geometries, it is difficult to know the exact number of molecules involved in a single nanoparticle–molecule(s)–nanoparticle unit.

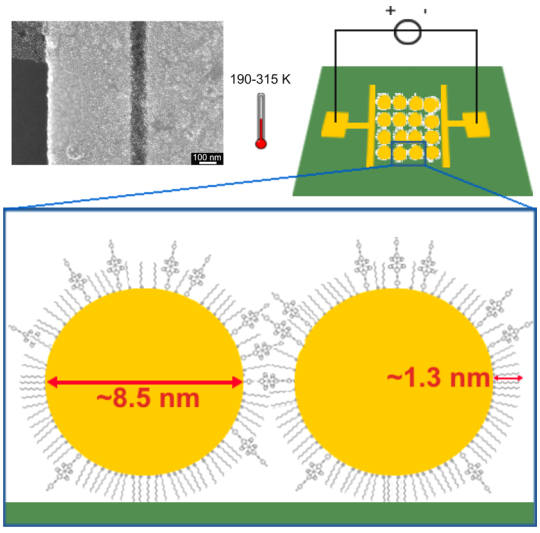

Figure 2. Micrograph (top left, SEM image; scale bar is 100 nm) and a schematic representation (top right) of a 2D molecule–gold nanoparticle array device (in reality, the gold nanoparticles are ordered in a triangular lattice). Bottom: schematic representation of a gold nanoparticle–molecule 1′/C8 molecule–gold nanoparticle junction on an insulating substrate, where 1′/C8 denotes a mixture of molecule 1′ and octanethiols.

This paper is organized as follows. After introducing sample preparation and basic experimental methods, we describe and discuss temperature-dependent Raman spectroscopy and magnetization measurements, respectively. These give evidence for a (partial) spin transition in arrays containing SCO molecules. Next, we present conductance experiments as a function of temperature, followed by single-molecule transport calculations. Finally, we show that the experimental conductance data are consistent with the combined Raman and magnetization results and with transport calculations. For this, we employ a simple percolation model that incorporates a temperature-dependent (partial) spin transition.

The method for the fabrication of a molecule **1**′–gold nanoparticle array is described in detail in the Supporting Information (see Figure S1). In short, spherical gold nanoparticles (8.5 ± 1.5 nm diameter) are synthesized in-house and modified with octanethiol molecules.[16,32] Next, they are made to self-assemble in an ordered array on a water surface. Such an array can be transferred to a substrate of choice by microcontact printing. For this study, we used glass, quartz, and Si–SiO_2 (see Supporting Information, Figures S2 and S3) substrates. Furthermore, we have transferred arrays to high-aspect-ratio nanotrench devices.[16,33,34] The latter are made by electron-beam lithography and consist of two wide electrodes (typical widths are ≈20 μm) that are separated by only ∼100 nm, to define a favorable aspect ratio. Figure 2 shows a SEM (scanning electron microscopy) micrograph

and a schematic of a typical device (see Supporting Information, Figure S4). In some cases, multiple stamping is performed to create layer-on-layer molecule–gold nanoparticle network devices. "Virgin" networks of octanethiol-covered gold nanoparticles are first characterized *via* charge transport measurements and UV–vis absorption spectroscopy. Subsequently, molecular exchange is performed by inserting a sample in a solution of **1** in acetonitrile (MeCN). UV–vis spectroscopy is used to determine if the molecular exchange process was successful. In the latter case, the surface plasmon resonance peak of the initial octanethiol–gold nanoparticle array shows a red shift after exchange, attributed to the increase in the dielectric constant experienced by the nanoparticles (see Supporting Information, Figure S5). In our study, we combine charge transport experiments with Raman spectroscopy and magnetization measurements. All three sets of experiments are performed as a function of temperature. Due to practical constraints, these experiments have been performed on different samples, all prepared in an identical manner. Finally, we note that sets of reference samples have been prepared to benchmark the data on SCO molecules. The first set is based on a similar exchange procedure but with dithiolated OPE (oligo(phenylene ethynylene)) molecules instead of the deprotected SCO complex molecule **1′**. For the second set, the nonmetalated S-BPP ligand (see Figure 1A) is used to coat the gold nanoparticles directly, after which array devices are created *via* self-assembly and microcontact printing.[16]

RESULTS

Temperature-Dependent Raman Spectroscopy Measurements. The arrayed nature of the gold nanoparticles and their small interparticle separation leads to a plasmon absorbance, which is resonant with the 633 nm light used to excite the samples for Raman spectroscopy. Therefore, the Raman spectrum of the 2D molecule **1′**–gold nanoparticle array is expected to be surface-enhanced (so-called surface-enhanced Raman spectroscopy (SERS)). Correspondingly, from comparison of the Raman spectra of the bulk powder of molecule **1** and the 2D molecule **1′**–gold nanoparticle array, it is evident that there are some very significant changes in the relative intensity and the vibrational frequencies of several key modes of the complex on gold nanoparticle binding. This technique, which provides a molecular fingerprint reflecting the structure of the adsorbed species, is ideally suited to detect the dominant SCO phase at a given temperature and provides insight into molecule–surface interactions.

Many of the observed changes are strongly reminiscent of our previous report on binding of the parent (*S*)-(4-{[2,6-(dipyrazol-1-yl)pyrid-4-yl]ethynyl}phenyl-)thioate (S-BPP) ligand at a gold nanoparticle array.[16] For example, the mode which dominates the SERS spectrum at 1574 cm^{-1} is attributed to the aryl in-plane C–C stretch mode of the benzenethiol moiety which is observed at approximately 1590 cm^{-1} in the unbound complex.[16,35] In the Raman spectrum of the SCO complex, this mode is superimposed on a more intense pyridine C–C stretch mode. The frequency shift and dramatic increase in intensity of this benzenethiol mode observed on nanoparticle binding of the SCO complex are analogous to the spectral behavior observed for the free AcS-BPP ligand when it was bound to a gold nanoparticle array and is strong evidence that the molecule **1′** is thiol-bound to the gold. Indeed, the dramatic relative increase in intensity of the 1574 cm^{-1} mode, along with other benzenethiol modes at 1078 and 406 cm^{-1}, is consistent with the surface enhancement of these signals due to proximity of the associated moieties to the plasmonic field of the nanoparticles, which would be expected if the complex is binding to the nanoparticles through the benzenethiol unit. A new feature evident at 321 cm^{-1} is tentatively attributed to the Au–S mode. Notably, the pyrazine and pyridine modes at 1619, 1381, and 1014 cm^{-1}, which dominate the Raman spectra of the bulk **1** powder, are considerably weaker compared with the benzenethiol features in the SERS spectrum. Therefore, the overall pattern of surface enhancement of the Raman spectral data indicates that molecule **1′** is thiol-bound and oriented largely normal to the gold nanoparticle surface, as indicated by the absence in comparable SERS enhancement in the pyrazine and pyridine modes.

The temperature-dependent Raman spectra of the bulk powder molecule **1** and a molecule **1′**–gold nanoparticle array were then compared over the temperature range 353 to 80 K, which encompasses the SCO transition in the bulk powder. The full temperature-dependent Raman spectra of the bulk SCO powder **1** are shown in Figures S6–S8 of the Supporting Information. They are strongly reminiscent of Raman spectral changes accompanying spin transition of a related iron complex.[17] Indeed, similar key markers of spin transition are observed. Most notably, in going from room to low temperature, the feature at 1014 cm^{-1} disappears and is replaced by a mode at 1039 cm^{-1}. From density functional theory (DFT) calculations, the peak at 1014 cm^{-1} is attributed to a pyridine ring-breathing mode whose motion is coupled strongly to the Fe(II)–N stretch. Correspondingly, the replacement feature at 1039 cm^{-1} is attributed to the analogous normal mode in the LS state. The intensity of the feature at 1014 cm^{-1} (integrated against a relatively temperature-independent mode at 1590 cm^{-1} from benzenethiol) is plotted against temperature in the inset of Figure S7 in the Supporting Information. This plot yields a sigmoidal curve that exhibits a transition temperature in excellent agreement with the magnetization data for bulk powder (see Figure 1B).

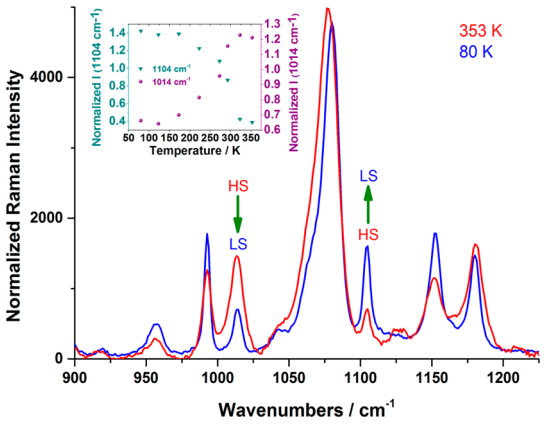

Figure 3. Raman spectra of a 2D molecule 1′—gold nanoparticle array at 353 and 80 K, excited at 633 nm (incident power 1.2 mW at the array) on a quartz substrate. Note that the mode at 1014 cm^{-1} increases with increasing temperature, whereas the mode at 1104 cm^{-1} decreases. Inset shows more detail on the intensity of these two modes, which are sensitive to the spin transition, as a function of temperature. Both modes are normalized to the 406 cm^{-1} benzenethiol mode which showed weak temperature dependence.

This result indicates that these Raman spectral changes can be attributed to spin transition (see also the Supporting Information). In addition, C—C stretch modes for the pyridine and pyrazine ligands, respectively, at 1589 and 1618 cm^{-1} change in relative intensity and shift to higher energy with decreasing temperature, consistent with strengthening of these bonds as the metal antibonding e_g* levels are vacated in the LS state of the SCO complex.

The influence of changing temperature on the SERS spectrum of the spin transition molecule **1**′ in the nanoparticle array (*i.e.*, 2D molecule **1**′—gold nanoparticle array) is less dramatic. This is a result of the domination of the SERS modes of the benzenethiol, which is not strongly influenced by temperature. Nonetheless, close inspection of modes associated with the iron complex shows that clear spectral changes occur with temperature in **1**′—gold nanoparticle arrays, as displayed in Figure 3 (see also Supporting Information, Table S1 and Figure S9).

Most tellingly, the major spectral changes occur between approximately 800 and 1200 cm^{-1} where, from DFT calculations, the majority of the coupled ligand-breathing/Fe—N vibrations occur. In particular, the band at 1014 cm^{-1}, identified as a marker of spin transition in the bulk material, decreases significantly at low temperature. In parallel, a feature at 1104 cm^{-1} increases in intensity. This mode is tentatively assigned to the LS state ligand ring-breathing coupled to Fe(II)—N bonds seen at 1039 cm^{-1} in the bulk SCO compound **1**, keeping in mind that unambiguous assignment of this mode is not possible without accompanying DFT calculations of the nanoparticle-bound complex. We note that, in addition, a weak feature at 1125 cm^{-1} decreases with decreasing temperature with concomitant grow-in of a feature at 1151 cm^{-1}. On the basis of DFT calculations, both are attributed to in-plane ring NCH stretch modes coupled to equatorial Fe—N stretch in the LS state. Interestingly, the alkyne C≡C stretching mode at 2207 cm^{-1} shifts to the blue by approximately 8 cm^{-1} at low temperature and sharpens significantly. Such behavior was observed previously in experiments where S-BPP ligands were incorporated in the nanoparticle arrays (*i.e.*, S-BPP—gold nanoparticle array), in the absence of iron,[16] and therefore this is not related to spin transition. It is important to note that some of the features observed in the molecule **1**′—gold nanoparticle array did not resolve in the bulk SCO material. This can be attributed to surface binding and SERS effect, which are expected to change both the selection rules and intensities of the modes observed.

All in all, evidence from Raman spectroscopy for persistence of spin transition in the gold-nanoparticle-bound metal complex is compelling, but the fact that the Raman spectral features associated with the low-spin and high-spin states are not completely lost at the most extreme temperature suggests that the transition is not as complete as was observed in the bulk. To provide better quantitative insight, the intensities of both the 1014 and 1104 cm^{-1} modes, which are markers of HS and LS states in the array, respectively, are plotted *versus* temperature for the normalized spectra (see inset of Figure 3). Their intensity values are given relative to a benzenethiol mode, used as a phase-independent temperature marker in the bulk powder. As shown in the inset of Figure 3, this reveals two sigmoidal curves, one growing in (the HS marker, *i.e.*, 1014 cm^{-1} mode) and one decreasing (the LS marker, *i.e.*, 1104 cm^{-1} mode), with a midpoint each of around 270 K. This temperature-dependent behavior correlates well with the magnetic data shown below and is consistently reminiscent of the behavior of the spin transition in the bulk powder.[19] The slope of the temperature dependence, weaker in the 2D molecule **1**′—gold nanoparticle array than in the bulk powder, may be attributed to the fact that a pure HS state is not completely achieved over the temperature range explored here, as indicated by residual features from the HS state at low *T* and *vice versa*. From the relative change to the integrated area under the features at 1014 and 1104 cm^{-1}, we can estimate what fraction of the SCO molecules undergoes spin transition, however, with significant uncertainty. The percentages we find are 65% (from 1014 cm^{-1} mode) and 80% (from 1104 cm^{-1} mode). The differences in the estimated areas are attributed to residual uncorrected background in the Raman spectra, which is stronger under the 1014 cm^{-1} band. We can say therefore that we obtain a minimum of 65% spin transition. It is important to note that the temperature-dependent changes to the Raman spectra of both the SCO bulk

powder **1** and molecule **1**′—gold nanoparticle array were fully reversible on restoring temperature to its original value. We do not find experimental indications of hysteresis in the spin transition; that is, the temperature sweeping direction does not matter.

We have benchmarked our findings on SCO transition by also performing temperature-dependent Raman spectroscopy on the reference C8—gold nanoparticle array (see Supporting Information, Figure S10). In contrast to the SCO spectra, little spectral change and no indication of transition are observed in the temperature dependent data: besides broadening out of features at high temperatures with an increase of the background, no clear shifts are observed in the few bands that are attendant in Figure S10.

In summary, temperature-dependent Raman spectroscopy provides evidence for a spin transition in the molecule **1**′—gold nanoparticle arrays and reveals that the molecules are bound to Au with their thiol group(s). However, unlike the bulk material, the transition does not appear to be complete, with a minority of the molecules not exhibiting a crossover.

Magnetization Measurements. Magnetic properties have been investigated to confirm the occurrence of a spin transition in the nanoparticle array. Three different samples are prepared by layer-on-layer deposition of C8—gold nanoparticle arrays onto quartz substrates of 10 × 6 mm size. Two of these samples are then exchanged with SCO molecules. The total magnetic moment of gold nanoparticle networks incorporating molecule **1**′ (spin transition samples **B** and **C** with different amounts of nanoparticles) as well as a reference sample **A** (containing octanethiols only) has been measured on a SQUID magnetometer under an applied magnetic field of 1 T, in the temperature range 90—400 K (see Figure 4).

All three samples contain predominantly diamagnetic material (quartz substrate, gold nanoparticle, and octanethiol (C8)). A diamagnetic signal is indeed detected for sample **C**. Because the diamagnetic response of samples **A** and **B** is most probably weaker than the signal coming from the nearby background signal environment of the sample position (tape and quartz), the signal is found to be paramagnetic for samples **A** and **B**.

In Figure 4, for the temperature range 100—200 K, the magnetic moment of both **B** and **C** samples remains rather constant, whereas it rises with increasing temperature in the 200—400 K range. Both curves show similar temperature-dependent behavior, indicating reproducibility. The reference sample **A** shows a different behavior, with magnetic moment diminishing with increasing temperatures. One can therefore tentatively attribute the increase of paramagnetism with temperature for samples **B** and **C** to the occurrence of a diamagnetic—paramagnetic spin transition. Consistent with the Raman data, measurements in both cooling and heating directions confirm the temperature reversibility. The lack of an abrupt spin transition with temperature is attributed to the diluted nature of SCO switching centers in the sample, leading to diminished cooperativity, and the absence of saturation at 400 K for nanoparticle samples confirms the partial nature of the spin transition.[36,37]

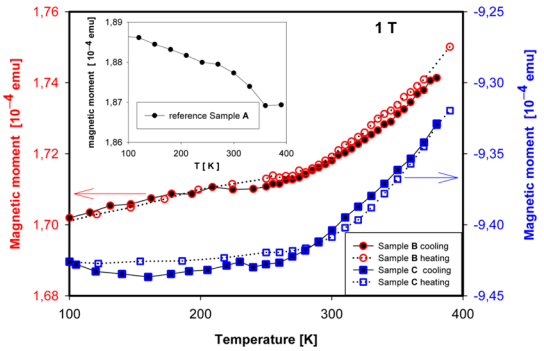

Figure 4. Temperature-dependent magnetization measurements on three gold nanoparticle network samples (on quartz substrates). For gold nanoparticle networks incorporating molecule 1′ (samples B and C), a clear change in magnetic moment is observed around 250 K, consistent with a partial spin transition. Inset: temperature-dependent magnetic moment of reference sample A, which contains a gold nanoparticle network with only octanethiol molecules. All magnetic measurements were carried out under a 1 T external magnetic field.

While care must be taken in the magnetic data interpretation due to the limited signal from the molecules of interest, the findings confirm the outcome of Raman data, with indications of a spin transition in nanoparticle arrays if molecule **1**′ is present, at temperatures comparable to those found on bulk SCO powders. The persistence of a spin transition in the networks opens the possibility to create a macroscopic device, providing insight into the influence of the transition at the molecular level on electrical properties.

Charge Transport Experiments. We have performed conductance measurements as a function of temperature on four types of samples, all made of molecular-bound nanoparticle arrays. Three are reference samples, containing "passive" molecules only (octanethiols, OPE-dithiols, and monothiolated "S-BPP ligands", *i.e.*, the uncoordinated AcS-BPP ligand used in the molecule **1** in Figure 1A).[16] For all of these, no transition is expected to occur with temperature. Hence, they provide reference temperature-dependent transport properties to be compared to the fourth sample type, which incorporates molecule **1**′. Figure 5A shows the low-bias resistance *R versus* temperature *T* for a C8—gold nanoparticle network (stamped three times, yielding 1—2 monolayers; see caption for details). Interestingly, for this "virgin" molecular device, a monotonically decreasing curve is observed that plateaus at higher *T*. We note that the (double layer of) alkanemonothiols form a tunnel barrier between neighboring nanoparticles. Transport through such a barrier is expected to be virtually

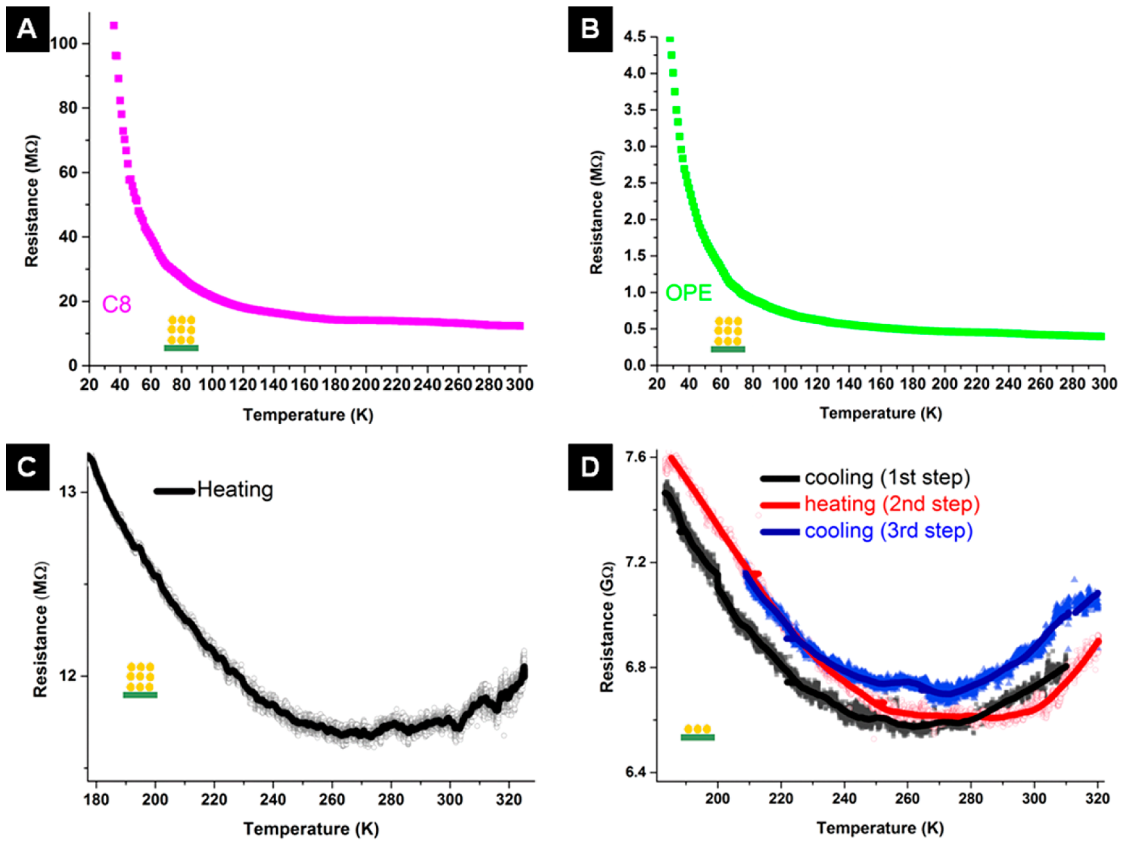

Figure 5. (A) Resistance *versus* temperature ($R-T$) measurement of a C8−gold nanoparticle network (stamped three times). (B) $R-T$ measurement of an OPE−gold nanoparticle array (stamped three times). (C) $R-T$ measurement of a molecule 1′−gold nanoparticle network (stamped three times). (D) $R-T$ measurement of a single-layer molecule 1′−gold nanoparticle array. All resistances are determined at low bias ($V \leq 0.3$ V) on nanotrench devices.[33]

temperature-independent. Hence, the temperature dependence observed in Figure 5A must be related to the properties of the nanoparticles. Indeed, it is a result of Coulomb blockade: due to the small size of the gold nanoparticles, a finite energy is required to add one electron to a nanoparticle. This "charging energy" E_C is connected to a nanoparticle's capacitance C and the electron charge e *via* $E_C = e^2/2C$. When the sample is cooled, the thermal energy k_BT can become lower than E_C. As a result, transport is increasingly blocked (Coulomb blockaded), and the resistance increases dramatically. This effect has been well-studied in networks, by us and others.[16,29,34,38,39] Figure 5B shows *R versus T* for a network sample (three times stamped) into which C8 molecules have been exchanged with OPE−dithiol bridges. Clearly, the presence of the conjugated OPE rods has led to a much lower device resistance. Qualitatively, however, the $R(T)$ behavior has not changed. Again, a monotonically decreasing curve is seen, with characteristics that are dominated by Coulomb blockade in the nanoparticles.[34,40]

For arrays and networks containing spin crossover molecule **1′**, however, the results are very different. Figure 5C shows *R versus T* for such a sample (three times stamped). In contrast to Figure 5A,B, the $R(T)$ plot in Figure 5C shows an upturn. This results in a rather shallow minimum, roughly stretching between 260 and 290 K. In addition, Figure 5D shows a $R(T)$ plot for a sample on which stamping was done only once, resulting in an imperfectly ordered single nanoparticle layer. Although this yields a much higher overall resistance value, the $R(T)$ curve remains qualitatively similar to the one in Figure 5C. Indeed, both panels C and D of Figure 5 exhibit a clear minimum. This behavior differs fundamentally not only from Figure 5A, B but also from our third reference systems, that is, networks containing the monothiolated BPP ligands. In the latter, the Fe(II) ion, which is key to the spin transition, is not present. For such samples, we find that R decreases monotonically with increasing T without showing a minimum (see Figure S11 and ref 16 for more details). Hence, the combination of all measurements suggests that the resistance minimum in Figure 5C,D is intimately related to the presence of SCO molecules and, specifically, to a temperature-dependent spin transition.

However, before accepting this hypothesis, we should consider an alternative explanation. Recently, Wang *et al.*[41] reported a variation in $R(T)$ behavior for multilayered arrays of octanethiol-covered Au nanoparticles, dependent on thickness. For samples containing up to four layers of 7 nm diameter nanoparticles, they find that $R(T)$ plots show a monotonic decrease.

From five layers upward, however, they observe a resistance minimum, an effect which they explain *via* a diffusive hopping model. For 13 nm particles, the latter border shifts to three layers. For this reason, it is important to emphasize that our reference samples (not only octanethiol, like Wang, but also OPE and bare S-BPP ligand arrays) do not yield a resistance minimum. This is fully consistent with the data set of Wang *et al.*, as our particles are 8.5 ± 1.5 nm in diameter, that is, close to 7 nm.[16] In contrast, we do observe a resistance minimum for samples that contain spin transition molecules. This is the case not only for triple-stamped samples but, importantly, also for arrays that were stamped only once (Figure 5D).

Hence, our full set of transport experiments, in combination with our Raman and magnetometry data, indicates that a spin transition in the SCO molecules is key to the anomalous $R(T)$ plots observed. If we also assume that the HS state has a higher low-bias resistance than its LS counterpart, as we will discuss below, we have the ingredients to explain the upturn. Upon heating around the transition temperature, more and more molecules will make the transition, and the resistance will increase. Still, Coulomb blockade will play its role too, as the charging energy E_C of the gold nanoparticles in Figure 5C,D should be similar to the values for Figure 5A,B (the nanoparticles and samples are made according to the very same procedure). Hence, for the lower temperatures, an increase of R upon cooling is also expected. A combination of Coulomb blockade and a spin transition could thus qualitatively explain the minimum observed in Figure 5C,D.

In the following, we combine DFT calculations of the electrical properties of these molecular junctions with a simple macroscopic percolative network model to provide a better insight into the $R(T)$ findings.

Charge Transport Calculations. Until now, theory is diverse on predicting how the conductance of SCO molecules would change during spin transition. Baadji *et al.*[42] found a resistance decrease when going from the LS to the HS state (*i.e.*, $R_H < R_L$) for a SCO molecule of their choice. Meded *et al.*,[15] on the other hand, predicted that the resistance is lowest in the LS state (*i.e.*, $R_H > R_L$), based on experimental findings on molecules more similar to the ones studied here. One reason for this discrepancy is that two competing effects can play a role upon a LS to HS transition. On the one hand, the energy gap between the frontier orbitals (HOMO−LUMO gap) decreases. This is expected to increase conductance, as the distance from the Fermi level to the nearest level will generally decrease, as well. On the other hand, the electronic coupling between the ligands at both sides of the Fe(II) ion decreases when going from the LS to HS state. In a first approximation, the related decrease in wave function overlap should reduce conductance. Hence, it is not *a priori* obvious if one should expect a conductance increase or decrease upon spin transition for a particular type of molecules.

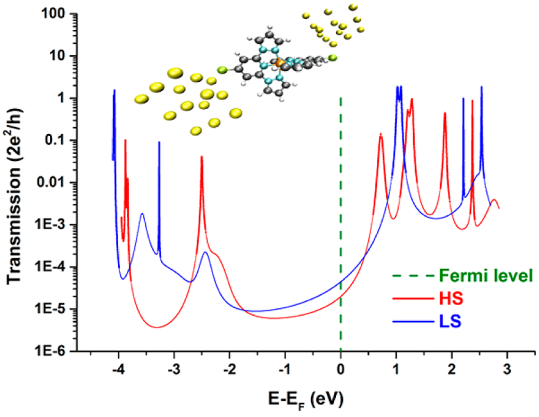

Figure 6. Calculated electron transmission probability as a function of energy, $T(E)$, for molecule 1′ in LS (blue curve) and HS (red curve) states. The inset shows the configuration considered (gold atoms are displayed in yellow). The conductance of the LS state is found to be higher than that of the HS state despite diminishing of the HOMO−LUMO gap upon LS to HS transition. Details of the calculation are described in the text.

For this reason, we specifically focus on calculating charge transport through molecule **1**′ connected to Au leads. We perform simulations of the transmission function by utilizing our in-house developed non-equilibrium Green's function (NEGF) formalism[43,44] based on DFT input coming from the quantum chemistry package Turbomole.[45−47] The formalism was successfully utilized earlier on a similar class of molecules,[48] using BP,[49,50] a standard generalized gradient approximation exchange-correlation (XC) functional. Here, however, we use B3LYP[51,52] as an XC functional to obtain the transmission functions for both the HS and LS state of the molecule **1**′ as presented in Figure 6.

Upon an admittedly rough comparison between experimentally obtained first optical excitations and HOMO−LUMO gaps produced with a few different XC functionals, one directly observes that BP's 0.3 eV is too small (by a factor of 4) when compared to the experimental lowest optical excitation of 1.3 eV.[53] B3LYP on the other hand produces 3.2 eV, a value too high by a factor of 2. $[Fe(TPY)_2]^{2+}$ (with TPY = 2,2′:6′,2″-terpyridine) showed very similar trends compared to molecule **1**′ (only slightly smaller) on the calculations side. It is worth noting that agreement across different XC functionals is much better for the LS state where the discrepancies never exceed 50% when compared to the lowest optical excitation of LS of $[Fe(TPY)_2]^{2+}$ found in experiment;[54] for details, see Table 6 in ref 15. We note that the $[Fe(TPY)_2]^{2+}$ complex is not known to switch in experiment.[55]

Indeed, we find that the HOMO−LUMO gap in the HS state tends to be smaller than that in the LS state for the corresponding XC functional. Consequently, the HS frontier orbitals tend to be closer to resonance with the

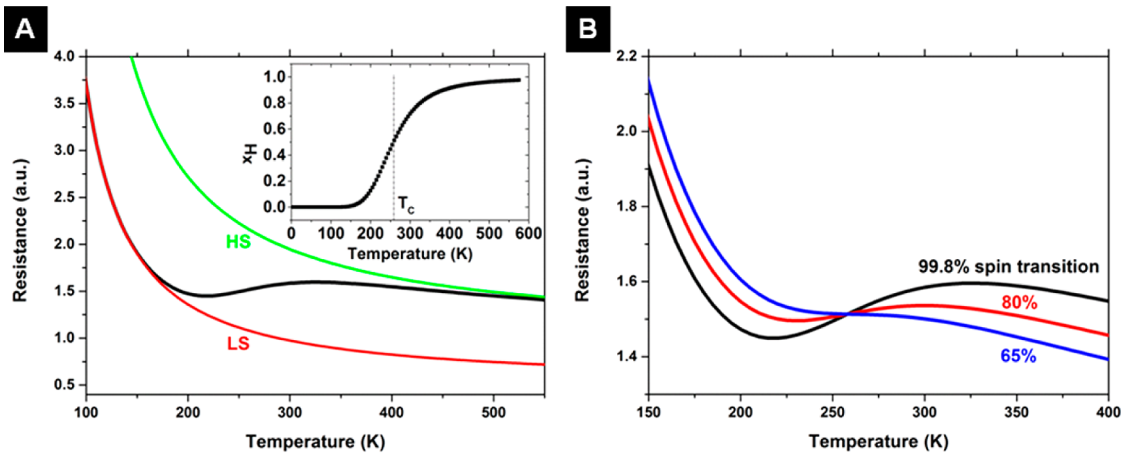

Figure 7. (A) General shape of the $R-T$ plot (black) calculated by a percolation network model (see main text). It assumes a spin transition without cooperative effects. A minimum is found for a nearly full spin transition, consistent with Figure 5C,D. The minimum can be rationalized as a transition between two $R(T)$ curves: one for the case that there were LS molecules only (red curve) and one for the case of only HS molecules (green curve). The HS molecules are assumed to have twice the resistance of the LS, consistent with DFT calculations (Figure 6). Inset: normalized number of molecules in the high-spin state, x_H *vs* T as used in the percolation model (see main text; parameters: $\Delta H/\Delta S = T_c = 258$ K and $\Delta H = 14.3$ kJ/mol,[56] resulting in a 99.8% transition). (B) Calculated $R(T)$ curves if spin crossover is incomplete: 65% (blue curve) or 80% (red curve). The black curve is the same as for (A). The resistance minimum remains for the 80% transition but disappears near the percolation threshold.

Fermi level E_F of the junction. From this, one might expect that the HS conductance exceeds the LS conductance, as anticipated above.[54] Figure 6 shows the calculated transmission function *versus* energy, $T(E)$, for both LS and HS states. The single molecular conductance G is related to $T(E)$ by $G = 2e^2/h \times T(E_F)$, where h denotes Planck's constant. Remarkably, although the transport gap in Figure 6 is indeed smaller for the HS state, the conductance (transmission) of the LS state is clearly the higher of the two. To understand this, we need to consider interligand coupling, as well. From Figure 6, we deduce that we dominantly have LUMO transport. Interestingly, the LUMO for these types of molecules is always ligand-based, and additionally, a ligand wave function has a better opportunity to couple to the gold leads. While spin transition does reshuffle the Fe states, it does not influence the ligand states as much. Still, it results in a distance increase between the left and right ligand. The latter makes interligand coupling considerably weaker. In Figure 6, we see indeed that the HS LUMO peak (red) is much narrower than the corresponding LS peak (blue). Additionally, the HS Lorentzian peaks well below unity, indicating very asymmetric coupling for the HS state case.

Summarizing, our calculations imply a conductance decrease when going from a LS to a HS state, explained by a reduction in coupling dominating over a decrease in the HOMO−LUMO gap. Keeping in mind differences in HOMO−LUMO gaps that different XC functionals are producing, however, a definite and general answer as to which of the two spin states is better conducting from a theory point of view is still difficult to give. This in itself emphasizes the need for more experimental data.

DISCUSSION

To relate all of the experimental evidence (Raman and magnetometry results on spin transition) as well as the transport calculations to the $R(T)$ plots in Figure 5C, D, we introduce a pragmatic model. In essence, it describes the influence of a spin transition on the device resistance R *via* a bond percolation model, assuming $R_H > R_L$ as in the NEGF results (Figure 6). Although the model captures the basic physics of our system, we note that it can at most be seen as semiquantitative. First, we estimate what percentage of molecules are in the LS and HS states for each temperature T. We choose to do this *via* a standard approach that captures the essence and allows us to vary parameters. Specifically, we take over the parameters $\Delta H = 14.3$ kJ/mol and $\Delta S = 55.4$ J/(mol K), from Šalitroš *et al.*,[56] who studied similar spin transition molecules in bulk. In contrast to bulk, however, we assume there is no cooperativity between the SCO molecules in the array. The normalized number of HS molecules x_H is then given by[7]

$$x_H(T) = \frac{1}{1 + \exp\left[\frac{\Delta H}{R_B}\left(\frac{1}{T} - \frac{1}{T_c}\right)\right]} \quad (1)$$

where $R_B = N_A \times k_B$ is the gas constant (N_A is Avogadro's number). Note that for any finite T_c, $x_H(T)$ does not fully reach unity for $T \rightarrow \infty$ in eq 1, although for our parameters, it does get to 0.998.

Next, we use a percolation model to calculate the total resistance of a 2D array, taking Coulomb blockade into account, as well. For this, we first make the pragmatic assumption that the resistance of a single

molecule−nanoparticle junction within an array is given by $R_{H(L)} = R^{\infty}_{H(L)}e^{(E_c/k_BT)}$, where R^{∞}_{H} and R^{∞}_{L} denote the single-molecule resistance for the high-spin (H) and low-spin (L) states, respectively, if there were no Coulomb blockade. We use the following normalized values: $R^{\infty}_{H} = 1 = 2 \times R^{\infty}_{L}$, inspired by our calculations in Figure 6. Furthermore, we assume that the charging energy of the nanoparticles E_C does not depend on the spin state of the molecule (we use E_C/k_B = 200 K, in correspondence with typical values for octanethiol and OPE networks).[34] To take percolation into account, we need to properly relate the device resistance R to x_H. For this, we make use of a model by McLachlan, which has successfully been applied to molecule−nanoparticle arrays in the literature.[40] It yields the following implicit equation (see eq 2) for the array conductance $G(x_H) = 1/R(x_H)$:

$$\frac{(1 - x_H)(G_L^{3/4} - G^{3/4})}{G_L^{3/4} + A_c G^{3/4}} + \frac{x_H(G_H^{3/4} - G^{3/4})}{G_H^{3/4} + A_c G^{3/4}} = 0 \qquad (2)$$

We set $G_H = 1/R_H$ and $G_L = 1/R_L$ and $A_c = (1 - p_c)/p_c$, where p_c denotes the percolation threshold, coming from the low conductance side. For a hexagonal network, we have $p_c = 2\sin(\pi/18) = 0.347$, so that $A_c = 1.88$.[57−61]

With these ingredients, we are ready to calculate $R(T) = R(x_H(T);T) = R(x_H(T)) \times e^{(E_c/k_BT)}$. Figure 7A shows the result (see black curve). For a system exhibiting a nearly full (99.8%) spin transition, we find that the array's $R(T)$ plot decreases to a minimum, goes up again, and slowly goes down to flatten off. The minimum has a depth of up to a few tens of a percent and is found around 220 K. This is qualitatively in agreement with our $R(T)$ data in Figure 5C,D. It is instructive to compare this curve to the plot expected if there were no spin transition at all, that is, if there were HS molecules only (described by $R_H = R^{\infty}_{H}e^{(E_c/k_BT)}$; see green curve in Figure 7A) or LS molecules only (given by $R_L = R^{\infty}_{L}e^{(E_c/k_BT)}$; see red curve in Figure 7A). Clearly, at low temperatures, the model's black curve follows the LS line, whereas it moves to the HS curve as the spin transition takes place. Since $R^{\infty}_{H} > R^{\infty}_{L}$, a minimum quite naturally appears. The details of the transition, however, are dictated by $x_H(T)$ and by the percolation model. Finally, Figure 7B shows how the $R(T)$ curve changes if the spin transition is partial only. Again, the black curve denotes a nearly full transition. The red and blue curves show R *versus* T for 80 and 65% spin transition, respectively, following the estimates from our Raman data. Comparing the curves, we see that a minimum is still there for the 80% transition. For the 65% case, which is near the percolation threshold (coming from the LS state side), the minimum has just disappeared, however. This shows how sensitive the presence of a resistance minimum is to the extent of the transition; that is, details of sample preparation will clearly be crucial to observe a resistance minimum. For instance, if molecular exchange is incomplete and/or if less than 65% of the molecular junctions switch, a minimum is not anticipated. This is consistent with the more monotonous curves observed for 4 out of 8 samples.

All in all, the $R(T)$ data in Figure 5C,D are qualitatively consistent with the Raman data, magnetometry measurements, and transport calculations, assuming that the transition involves more than 2/3 of the molecules.

CONCLUSIONS

In summary, we have experimentally studied the properties of gold nanoparticle arrays incorporating spin crossover molecules. Raman spectroscopy provides evidence for a (majority) spin transition in these arrays, as qualitatively confirmed by magnetization measurements. The Raman data indicate that molecular binding to gold occurs *via* benzenethiol termini. Still, it does not appear that the proximity and binding to the metal quenches the spin transition. Resistance *versus* temperature curves for arrays containing SCO molecules exhibit a pronounced minimum that we do not find in networks containing nonswitching, passive molecules only. This resistance minimum can be explained *via* a percolation model that assumes a spin transition with the HS state being more resistive than the LS state. The latter is in agreement with charge transport calculations presented following the NEGF method.

Even though the electrical signature of a spin transition is not spectacular in our case, the proposed model provides a guideline to pinpoint the occurrence of a spin transition with temperature in an electrical device. Our work thus demonstrates that proof-of-principle molecular devices based on the spin crossover phenomenon can be designed.

METHODS

Sample Preparation. Monodispersed spherical 8.5 ± 1.5 nm (diameter) gold nanoparticles have been synthesized according to methods previously described.[16,36] These gold nanoparticles are functionalized by octanethiol (C8) molecules in pure ethanol. The C8−gold nanoparticles are self-assembled into a 2D array *via* a Langmuir−Schaefer technique. The C8−gold nanoparticle array is microcontact-printed *via* polydimethylsiloxane stamps on various types of substrates. Finally, samples are molecularly exchanged for 4 days in a 0.5 mM **1** molecule solution in acetonitrile. After being washed, rinsed, and dried, these samples are ready for characterization and measurements (see Supporting Information).

Raman Spectroscopy. Molecule **1′**−gold nanoparticle arrays on both glass and quartz substrates were used to perform Raman spectroscopic analyses with a Horiba Jobin-Yvon Labram HR instrument. Temperature-dependent Raman analyses of these samples (four in total) were done *via* use of a temperature stage

that can be cooled with liquid nitrogen (see Supporting Information).

Magnetization Measurements. A SQUID magnetometer (MPMS-XL-7 Quantum Design) is used to measure the magnetization as a function of temperature (90−400 K) on multilayered (>3 layers) octanethiol−gold nanoparticles (*i.e.*, reference sample) and molecule **1′**−gold nanoparticles networks (three samples). Such a network (sizes: 5 × 5 mm) was microcontact-printed on a quartz substrate (10 × 6 mm). This sample was connected to the sample holder of the SQUID with the use of Kapton tape (see the magnetization measurements section and the Supporting Information).

Charge Transport Measurements. All measurements on molecule **1′**−gold nanoparticle arrays and networks were done using nanotrench devices (the same holds for the reference samples). These devices (eight in total) were inserted into a liquid helium bath cryostat to perform temperature-dependent electrical measurements, as shown in Figure 5 and in Figure S11. In Figure 5C,D, we show both an averaged curve and (a random 10% part of the) raw data (320 data points per Kelvin). See experimental section and Supporting Information.

Conflict of Interest: The authors declare no competing financial interest.

Acknowledgment. This work is based on the program INTERNET, supported *via* the NanoSci-E+ ERA scheme, a European initiative that has been at the basis of this collaboration. We thank F. Schramm and S. Kuppusamy from KIT (INT) for their support during the synthesis of SCO molecules for project INTERNET, and the STnano facility for nanofabrication. Partial financial support of the Agence Nationale de la Recherche (Labex NIE 11-LABX-0058_NIE within the Investissement d'Avenir program ANR-10-IDEX-0002-02) (M.R.), the Science Foundation Ireland for funding under Grant No. 10/IN.1/B3025 (U.P. and T.K.), the NBIPI Career Enhancement and Mobility Fellowship co-funded by Marie Curie Actions (T.L. and T.K.), the Slovak grant agency: VEGA 1/0522/14 (I.Š.), and the Netherlands Organisation for Scientific Research, NWO, for support *via* a VIDI grant (S.J.M.) is gratefully acknowledged.

Supporting Information Available: Synthesis details, experimental methods, and additional control experiments. This material is available free of charge *via* the Internet at http://pubs.acs.org.

REFERENCES AND NOTES

1. Aviram, A.; Ratner, M. A. Molecular Rectifiers. *Chem. Phys. Lett.* **1974**, *29*, 277–283.
2. Metzger, R. M. Unimolecular Electrical Rectifiers. *Chem. Rev.* **2003**, *103*, 3803–3834.
3. Feringa, B. L. *Molecular Switches*; Wiley-VCH: Weinheim, Germany, 2001.
4. Gütlich, P., Goodwin, H. A., Eds. *Spin Crossover in Transition Metal Compounds I*; Springer: Berlin, 2004; Vol. 233.
5. Ruben, M.; Rojo, J.; Romero-Salguero, F. J.; Uppadine, L. H.; Lehn, J.-M. Grid-Type Metal Ion Architectures: Functional Metallosupramolecular Arrays. *Angew. Chem., Int. Ed.* **2004**, *43*, 3644–3662.
6. Van der Molen, S. J.; Liljeroth, P. Charge Transport through Molecular Switches. *J. Phys.: Condens. Matter.* **2010**, *22*, 133001.
7. Kahn, O. *Molecular Magnetism*; Wiley: New York, 1993.
8. Gütlich, P.; Garcia, Y.; Goodwin, H. A. Spin Crossover Phenomena in Fe(II) Complexes. *Chem. Soc. Rev.* **2000**, *29*, 419–427.
9. Gütlich, P.; Hauser, A. Thermal and Light-Induced Spin Crossover in Iron(II) Complexes. *Coord. Chem. Rev.* **1990**, *97*, 1–22.
10. Hauser, A. Reversibility of Light-Induced Excited Spin State Trapping in the $Fe(Ptz)_6(BF_4)_2$ and the $Zn_{1-x}Fe_x(Ptz)_6(BF_4)_2$ Spin-Crossover Systems. *Chem. Phys. Lett.* **1986**, *124*, 543–548.
11. Marchivie, M.; Guionneau, P.; Howard, J. A. K.; Chastanet, G.; Létard, J.-F.; Goeta, A. E.; Chasseau, D. Structural Characterization of a Photoinduced Molecular Switch. *J. Am. Chem. Soc.* **2002**, *124*, 194–195.
12. Kato, K.; Takata, M.; Moritomo, Y.; Nakamoto, A.; Kojima, N. On−Off Optical Switching of the Magnetic and Structural Properties in a Spin-Crossover Complex. *Appl. Phys. Lett.* **2007**, *90*, 201902.
13. Bousseksou, A.; Molnár, G.; Tuchagues, J.-P.; Menéndez, N.; Codjovi, É.; Varret, F. Triggering the Spin-Crossover of $Fe(Phen)_2(NCS)_2$ by a Pressure Pulse: Pressure and Magnetic Field Induced 'Mirror Effects'. *C. R. Chimie* **2003**, *6*, 329–335.
14. Baadji, N.; Piacenza, M.; Tugsuz, T.; Della Sala, F.; Maruccio, G.; Sanvito, S. Electrostatic Spin Crossover Effect in Polar Magnetic Molecules. *Nat. Mater.* **2009**, *8*, 813–817.
15. Meded, V.; Bagrets, A.; Fink, K.; Chandrasekar, R.; Ruben, M.; Evers, F.; Bernand-Mantel, A.; Seldenthuis, J. S.; Beukman, A.; Van der Zant, H. S. J. Electrical Control over the Fe(II) Spin Crossover in a Single Molecule: Theory and Experiment. *Phys. Rev. B* **2011**, *83*, 245415.
16. Devid, E. J.; Martinho, P. N.; Kamalakar, M. V.; Prendergast, Ú.; Kübel, C.; Lemma, T.; Dayen, J.-F.; Keyes, T. E.; Doudin, B.; Ruben, M.; et al. The Influence of Molecular Mobility on the Properties of Networks of Gold Nanoparticles and Organic Ligands. *Beilstein J. Nanotechnol.* **2014**, *5*, 1664–1674.
17. Cavallini, M.; Bergenti, I.; Milita, S.; Kengne, J. C.; Gentili, D.; Ruani, G.; Šalitroš, I.; Meded, V.; Ruben, M. Thin Deposits and Patterning of Room-Temperature-Switchable One-Dimensional Spin-Crossover Compounds. *Langmuir* **2011**, *27*, 4076–4081.
18. Arcis-Castíllo, Z.; Zheng, S.; Siegler, M. A.; Roubeau, O.; Bedoui, S.; Bonnet, S. Tuning the Transition Temperature and Cooperativity of Bapbpy-Based Mononuclear Spin-Crossover Compounds: Interplay between Molecular- and Crystal-Engineering. *Chem.—Eur. J.* **2011**, *17*, 14826–14836.
19. Chandrasekar, R.; Schramm, F.; Fuhr, O.; Ruben, M. An Iron(II) Spin-Transition Compound with Thiol Anchoring Groups. *Eur. J. Inorg. Chem.* **2008**, *17*, 2649–2653.
20. Šalitroš, I.; Fuhr, O.; Eichhöfer, A.; Kruk, R.; Pavlik, J.; Dlháň, L.; Boča, R.; Ruben, M. The Interplay of Iron(II) Spin Transition and Polymorphism. *Dalton Trans.* **2012**, *41*, 5163–5171.
21. Gopakumar, T. G.; Matino, F.; Naggert, H.; Bannwarth, A.; Tuczek, F.; Berndt, R. Electron-Induced Spin Crossover of Single Molecules in a Bilayer on Gold. *Angew. Chem., Int. Ed.* **2012**, *51*, 6262–6266.
22. Miyamachi, T.; Gruber, M.; Davesne, V.; Bowen, M.; Boukari, S.; Joly, L.; Scheurer, F.; Rogez, G.; Yamada, T. K.; Ohresser, P.; et al. Robust Spin Crossover and Memristance Across a Single Molecule. *Nat. Commun.* **2012**, *3*, 1–6.
23. Pronschinske, A.; Bruce, R. C.; Lewis, G.; Chen, Y.; Calzolari, A.; Buongiorno-Nardelli, M.; Shultz, D. A.; You, W.; Dougherty, D. B. Iron(II) Spin Crossover Films on Au(111): Scanning Probe Microscopy and Photoelectron Spectroscopy. *Chem. Commun.* **2013**, *49*, 10446–10452.
24. Bernien, M.; Wiedemann, D.; Hermanns, C. F.; Krüger, A.; Rolf, D.; Kroener, W.; Müller, P.; Grohmann, A.; Kuch, W. Spin Crossover in a Vacuum-Deposited Submonolayer of a Molecular Iron(II) Complex. *J. Phys. Chem. Lett.* **2012**, *3*, 3431–3434.
25. Zhang, X.; Palamarciuc, T.; Létard, J.-F.; Rosa, P.; Lozada, E. V.; Torres, F.; Rosa, L. G.; Doudin, B.; Dowben, P. A. The Spin State of a Molecular Adsorbate Driven by the Ferroelectric Substrate Polarization. *Chem. Commun.* **2014**, *50*, 2255–2257.
26. Suleimanov, I.; Costa, J. S.; Molnár, G.; Salmon, L.; Bousseksou, A. The Photo-thermal Plasmonic Effect in Spin Crossover@Silica−Gold Nanocomposites. *Chem. Commun.* **2014**, *50*, 13015–13018.
27. Warner, B.; Oberg, J. C.; Gill, T. G.; El Hallak, F.; Hirjibehedin, C. F.; Serri, M.; Heutz, S.; Arrio, M.-A.; Sainctavit, P.; Mannini, M.; et al. Temperature- and Light-Induced Spin Crossover Observed by X-ray Spectroscopy on Isolated Fe(II) Complexes on Gold. *J. Phys. Chem. Lett.* **2013**, *4*, 1546–1552.

28. Andres, R. P.; Bielefeld, J. D.; Henderson, J. I.; Janes, D. B.; Kolagunta, V. R.; Kubiak, C. P.; Mahoney, W. J.; Osifchin, R. G. Self-Assembly of a Two-Dimensional Superlattice of Molecularly Linked Metal Clusters. *Science* **1996**, *273*, 1690–1693.
29. Tran, T. B.; Beloborodov, I. S.; Lin, X. M.; Bigioni, T. P.; Vinokur, V. M.; Jaeger, H. M. Multiple Cotunneling in Large Quantum Dot Arrays. *Phys. Rev. Lett.* **2005**, *95*, 076806.
30. Liao, J.; Bernard, L.; Langer, M.; Schönenberger, C.; Calame, M. Reversible Formation of Molecular Junctions in 2D Nanoparticle Arrays. *Adv. Mater.* **2006**, *18*, 2444–2447.
31. Bernard, L.; Kamdzhilov, Y.; Calame, M.; Van der Molen, S. J.; Liao, J.; Schönenberger, C. Spectroscopy of Molecular Junction Networks Obtained by Place Exchange in 2D Nanoparticle Arrays. *J. Phys. Chem. C* **2007**, *111*, 18445–18450.
32. Slot, J. W.; Geuze, H. J. A New Method of Preparing Gold Probes for Multiple-Labeling Cytochemistry. *Eur. J. Cell Biol.* **1985**, *38*, 87–93.
33. Dayen, J.-F.; Faramarzi, V.; Pauly, M.; Kemp, N. T.; Barbero, M.; Pichon, B. P.; Majjad, H.; Begin-Colin, S.; Doudin, B. Nanotrench for Nano and Microparticle Electrical Interconnects. *Nanotechnology* **2010**, *21*, 335303.
34. Dayen, J.-F.; Devid, E.; Kamalakar, M. V.; Golubev, D.; Guédon, C.; Faramarzi, V.; Doudin, B.; Van der Molen, S. J. Enhancing the Molecular Signature in Molecule–Nanoparticle Networks *via* Inelastic Cotunneling. *Adv. Mater.* **2013**, *25*, 400–404.
35. Biggs, K. B.; Camden, J. P.; Anker, J. N.; Van Duyne, R. P. Surface-Enhanced Raman Spectroscopy of Benzenethiol Adsorbed from the Gas Phase onto Silver Film over Nanosphere Surfaces: Determination of the Sticking Probability and Detection Limit Time. *J. Phys. Chem. A* **2009**, *113*, 4581–4586.
36. Larionova, J.; Salmon, L.; Guari, Y.; Tokarev, A.; Molvinger, K.; Molnár, G.; Bousseksou, A. Towards the Ultimate Size Limit of the Memory Effect in Spin-Crossover Solids. *Angew. Chem., Int. Ed.* **2008**, *47*, 8236–8240.
37. Coronado, E.; Galán-Mascarós, J. R.; Monrabal-Capilla, M.; García-Martínez, J.; Pardo-Ibáñez, P. Bistable Spin-Crossover Nanoparticles Showing Magnetic Thermal Hysteresis near Room Temperature. *Adv. Mater.* **2007**, *19*, 1359–1361.
38. Tran, T. B.; Beloborodov, I. S.; Hu, J.; Lin, X. M.; Rosenbaum, T. F.; Jaeger, H. M. Sequential Tunneling and Inelastic Cotunneling in Nanoparticle Arrays. *Phys. Rev. B* **2008**, *78*, 075437.
39. Pauly, M.; Dayen, J.-F.; Golubev, D.; Beaufrand, J.-B.; Pichon, B. P.; Doudin, B.; Bégin-Colin, S. Co-tunneling Enhancement of the Electrical Response of Nanoparticle Networks. *Small* **2012**, *8*, 108–115.
40. Liao, J.; Blok, S.; Van der Molen, S. J.; Diefenbach, S.; Holleitner, A. W.; Schönenberger, C.; Vladyka, A.; Calame, M. Ordered Nanoparticle Arrays Interconnected by Molecular Linkers: Electronic and Optoelectronic Properties. *Chem. Soc. Rev.* **2014**, 1–16.
41. Wang, Y.; Guan, C.; Sun, J.; Peng, L.; Liao, J. Transition of Temperature Coefficient of Conductance in Weakly Coupled Gold Nanoparticle Arrays. *Appl. Phys. Lett.* **2014**, *105*, 233116.
42. Baadji, N.; Sanvito, S. Giant Resistance Change across the Phase Transition in Spin-Crossover Molecules. *Phys. Rev. Lett.* **2012**, *108*, 217201.
43. Evers, F.; Weigend, F.; Köntopp, M. Conductance of Molecular Wires and Transport Calculations Based on Density-Functional Theory. *Phys. Rev. B* **2004**, *69*, 235411.
44. Arnold, A.; Weigend, F.; Evers, F. Quantum Chemistry Calculations for Molecules Coupled to Reservoirs: Formalism, Implementation, and Application to Benzenedithiol. *J. Chem. Phys.* **2007**, *126*, 174101.
45. Ahlrichs, R.; Bär, M.; Häser, M.; Horn, H.; Kölmel, C. Electronic Structure Calculations on Workstation Computers: The Program System Turbomole. *Chem. Phys. Lett.* **1989**, *162*, 165–169.
46. Schäfer, A.; Horn, H.; Ahlrichs, R. Fully Optimized Contracted Gaussian Basis Sets for Atoms Li to Kr. *J. Chem. Phys.* **1992**, *97*, 2571–2577.
47. Schäfer, A.; Huber, C.; Ahlrichs, R. Fully Optimized Contracted Gaussian Basis Sets of Triple Zeta Valence Quality for Atoms Li to Kr. *J. Chem. Phys.* **1994**, *100*, 5829–5835.
48. Ruben, M.; Landa, A.; Lörtscher, E.; Riel, H.; Mayor, M.; Görls, H.; Weber, H. B.; Arnold, A.; Evers, F. Charge Transport through a Cardan-Joint Molecule. *Small* **2008**, *4*, 2229–2235.
49. Perdew, J. P. Density-Functional Approximation for the Correlation Energy of the Inhomogeneous Electron Gas. *Phys. Rev. B* **1986**, *33*, 8822–8824.
50. Becke, A. D. Density-Functional Exchange-Energy Approximation with Correct Asymptotic Behavior. *Phys. Rev. A* **1988**, *38*, 3098–3100.
51. Lee, C.; Yang, W.; Parr, R. G. Development of the Colle-Salvetti Correlation-Energy Formula into a Functional of the Electron Density. *Phys. Rev. B* **1988**, *37*, 785–789.
52. Becke, A. D. Density-Functional Thermochemistry. III. The Role of Exact Exchange. *J. Chem. Phys.* **1993**, *98*, 5648–5652.
53. Holland, J. M.; McAllister, J. A.; Kilner, C. A.; Thornton-Pett, M.; Bridgeman, A. J.; Halcrow, M. A. Stereochemical Effects on the Spin-State Transition Shown by Salts of $[FeL_2]^{2+}$ [L = 2,6-Di(pyrazol-1-yl)pyridine]. *J. Chem. Soc., Dalton Trans.* **2002**, 548–554.
54. Braterman, P. S.; Song, J.-I.; Peacock, R. D. Electronic Absorption Spectra of the Iron(II) Complexes of 2,2′-Bipyridine, 2,2′-Bipyrimidine, 1,10-Phenanthroline, and 2,2′:6′,2″-Terpyridine and Their Reduction Products. *Inorg. Chem.* **1992**, *31*, 555–559.
55. Gerloch, M.; Constable, E. C. *Transition Metal Chemistry: The Valence Shell in d-Block Chemistry*; Wiley-VCH: Weinheim, Germany, 1994.
56. Šalitroš, I.; Pavlik, J.; Boča, R.; Fuhr, O.; Rajadurai, C.; Ruben, M. Supramolecular Lattice-Solvent Control of Iron(II) Spin Transition Parameters. *CrystEngComm* **2010**, *12*, 2361–2368.
57. Kirkpatrick, S. Percolation and Conduction. *Rev. Mod. Phys.* **1973**, *45*, 574–588.
58. McLachlan, D. S.; Blaszkiewicz, M.; Newnham, R. E. Electrical Resistivity of Composites. *J. Am. Ceram. Soc.* **1990**, *73*, 2187–2203.
59. Wu, J.; McLachlan, D. S. Percolation Exponents and Thresholds Obtained from the Nearly Ideal Continuum Percolation System Graphite–Boron Nitride. *Phys. Rev. B* **1997**, *56*, 1236–1248.
60. Lebovka, N. I.; Tarafdar, S.; Vygornitskii, N. V. Computer Simulation of Electrical Conductivity of Colloidal Dispersions during Aggregation. *Phys. Rev. E* **2006**, *73*, 031402.
61. Wierman, J. C. Bond Percolation on Honeycomb and Triangular Lattices. *Adv. Appl. Probab.* **1981**, *13*, 298–313.